



HAL
open science

Enhancing Near Infrared II Emission of Gold Nanoclusters via Encapsulation in Small Polymer Nanoparticles

Lucie Haye, P. Iyanu Diriwari, Abdallah Alhalabi, Thibault Gallavardin, Antoine Combes, Andrey Klymchenko, Niko Hildebrandt, Xavier Le Guével, Andreas Reisch

► **To cite this version:**

Lucie Haye, P. Iyanu Diriwari, Abdallah Alhalabi, Thibault Gallavardin, Antoine Combes, et al.. Enhancing Near Infrared II Emission of Gold Nanoclusters via Encapsulation in Small Polymer Nanoparticles. *Advanced Optical Materials*, 2022, pp.2201474. 10.1002/adom.202201474 . hal-03814454

HAL Id: hal-03814454

<https://normandie-univ.hal.science/hal-03814454>

Submitted on 21 May 2024

HAL is a multi-disciplinary open access archive for the deposit and dissemination of scientific research documents, whether they are published or not. The documents may come from teaching and research institutions in France or abroad, or from public or private research centers.

L'archive ouverte pluridisciplinaire **HAL**, est destinée au dépôt et à la diffusion de documents scientifiques de niveau recherche, publiés ou non, émanant des établissements d'enseignement et de recherche français ou étrangers, des laboratoires publics ou privés.

Enhancing Near Infrared II Emission of Gold Nanoclusters via Encapsulation in Small Polymer Nanoparticles

Lucie Haye, P. Iyanu Diriwari, Abdallah Alhalabi, Thibault Gallavardin, Antoine Combes, Andrey S. Klymchenko, Niko Hildebrandt,* Xavier Le Guével,* and Andreas Reisch*

Reduced scattering and autofluorescence in the second near-infrared window (NIR-II, 1000–1700 nm) hold the promise of high-resolution photoluminescence (PL) in vivo imaging at depths well beyond the μm scale. Yet, contrast agents with bright emission in this spectral region remain limited. Ultrasmall gold nanoclusters (AuNCs) are of particular interest for NIR-II PL imaging. However, they exhibit limited brightness. Here, high amounts of NIR-II emitting AuNCs are encapsulated in small polymer nanoparticles (NPs) made of poly(ethyl methacrylates). Using nanoprecipitation, loadings of up to 50 wt% can be reached, corresponding to over 10 000 AuNCs per 60 nm NP. PL quantum yields up to 1.3% and NP brightnesses up to $3.8 \times 10^6 \text{ M}^{-1} \text{ cm}^{-1}$ are accomplished. Increasing inter-AuNC interactions at higher loading result in a bathochromic shift of the PL emission. According to time-resolved PL measurements, this can be attributed to distinct inter-AuNC energy transfer pathways between the core and surface-centered PL modes. Evaluation of the nanohybrids in tissue-mimicking models for in vivo blood vessel imaging shows that the ultrabright and red-shifted NIR-II PL results in significantly improved detection sensitivity and resolution, which makes AuNC-loaded polymer NPs highly promising candidates for advanced in vivo imaging.

major advances in biology and medicine.^[1] However, the strong autofluorescence, absorption, and scattering of cells and tissues still strongly limit the achievable resolutions at depths beyond the μm scale.^[2] A solution to overcome these obstacles is shifting the observation wavelengths to the second near-infrared window (NIR-II) between 1000 and 1700 nm, which is also known as shortwave infrared (SWIR). Light in this wavelength range can penetrate deeper into tissues due to reduced scattering.^[3] Autofluorescence is also negligible compared to the visible or NIR region,^[4] making it possible to enhance the signal-to-noise ratio (SNR) and thus achieving high spatial and temporal imaging resolution.^[5] Despite intense efforts over the last years, contrast agents for this wavelength region remain limited: organic dyes typically have very low quantum yields (QYs) and brightness in this spectral region.^[6] In consequence, different types of luminescent nanoparticles


(NPs) have been designed, notably lanthanide-based NPs and quantum dots (QDs).^[7] Recently, conjugated polymer-based NPs emitting in the NIR-II have been described with an emission up to 1400 nm.^[8] The few examples of organic NIR-II

1. Introduction

Luminescence is widely used for biological imaging from the molecular to the whole animal level and has contributed to

L. Haye, A. Combes, A. S. Klymchenko, A. Reisch
Université de Strasbourg
CNRS
Laboratoire de Bioimagerie et Pathologies UMR 7021
Strasbourg F-67000, France
E-mail: reisch@unistra.fr
P. I. Diriwari, T. Gallavardin, N. Hildebrandt
Laboratoire COBRA (UMR6014 & FR3038)
Université de Rouen Normandie
CNRS
INSA
Normandie Université
Rouen 76000, France
E-mail: niko.hildebrandt@univ-rouen.fr

A. Alhalabi, X. Le Guével
Cancer Targets & Experimental Therapeutics
Institute for Advanced Biosciences (IAB)
University of Grenoble Alpes (UGA)/INSERM-U1209/CNRS-UMR,
5309 Grenoble
Grenoble, France
E-mail: xavier.le-guevel@univ-grenoble-alpes.fr
N. Hildebrandt
Department of Chemistry
Seoul National University
Seoul 08826, South Korea

 The ORCID identification number(s) for the author(s) of this article can be found under <https://doi.org/10.1002/adom.202201474>.

© 2022 The Authors. Advanced Optical Materials published by Wiley-VCH GmbH. This is an open access article under the terms of the Creative Commons Attribution License, which permits use, distribution and reproduction in any medium, provided the original work is properly cited.

DOI: 10.1002/adom.202201474

dyes encapsulated in polymers resulted in rather large objects (>100 nm).^[9] In general, the brightness of these probes, corresponding to the absorption coefficient multiplied by the QY, remains low, and developing more efficient NIR-II probes is a crucial challenge.

An intriguing class of luminescent materials, developed over the last two decades, are ultrasmall gold nanoclusters (AuNCs) with core sizes below 3 nm, made-up of several tens of Au-atoms most often stabilized with thiolated ligands.^[10] Both, the Au(0) core as well as charge transfer states involving the ligands contribute to their photoluminescence (PL) emission, but the precise mechanism is still under debate.^[11] Interestingly, several members of the AuNC family emit in the NIR-II region,^[12] and they have been recently employed for protein tracking, blood vessel imaging, and molecular imaging.^[13] The ligand shell (nature of the ligand, rigidity) has a profound influence on the emission properties, notably in view of achieving emission in the NIR-II,^[12a,14] but determines also the solubility properties and interactions with the biological media.^[14,15] Thus, a compromise must be found between the emission properties of the probe and its biocompatibility. A possible approach to decouple surface and emission properties is to encapsulate AuNCs into polymer NPs, such that the ligands are not in contact with the media and only modulate the AuNC emission, while the interface is controlled by the polymer. A second advantage of encapsulation of high amounts of NIR-II-emitting AuNCs in polymer NPs would be a significant enhancement of the overall brightness, as the individual clusters are combined in one probe.

In the case of AuNCs emitting in the visible or NIR-I, encapsulation in nano-objects has been achieved, for example, in silica nanospheres,^[16] proteins,^[17] and metal-organic frameworks (MOFs).^[18] AuNCs were also encapsulated in polymers, because the latter are in some case biocompatible^[19] or can be designed^[20] to obtain specific properties. However, these approaches have not been extended to nanoclusters emitting in the SWIR/NIR-II region. Furthermore, even for visible or NIR-I emitting AuNCs, a pertinent comparison of the concentration of encapsulated AuNCs is difficult due to a wide range of used NP sizes (from below 20 to 500 nm) and the different ways to express amounts of loading with AuNCs. Typically, these loadings and numbers of nanoclusters per NP remained limited and, to the best of our knowledge, the influence of the loading for a given system has never been investigated. However, both, high loadings with NIR-II emitting AuNCs and studying the influence of loading, would be of particular interest for designing very bright NIR-II contrast agents. Indeed, at high concentrations, luminescent emitters frequently undergo one of two opposed phenomena: aggregation-induced emission (AIE) and aggregation-caused quenching (ACQ).^[21] If the first is somewhat positive in the design of bright objects,^[22] the second implies that there is a limit above which the brightness of the NP decreases with increasing AuNC concentration.

In the present work, we assembled monodispersed nano-hybrids, that is polymer NPs encapsulating NIR-II-emitting AuNCs at loadings up to 50 wt%, through nanoprecipitation with the aim to accomplish bright NIR-II fluorescent nano-probes. By controlling both the size of NPs and the concentration of encapsulated AuNCs, it was possible to evaluate and control the number of AuNCs per NP and to vary the distance

between the AuNCs. This opened the possibility to study the influence of the local concentration and distance of NIR-II AuNCs on their photophysical properties. In particular, a progressive shift of the PL emission to longer wavelengths was observed with increased loading. Multi-wavelength PL lifetime measurements allowed us to assign this redshift to increasing interactions between the AuNCs within the NPs. To quantify the potential sensitivity and resolution of these NIR-II nano-hybrids in biological media, we imaged them in capillaries at different depths of tissue models. In combination with reduced absorption and scattering in the NIR-II, the high NIR-II PL brightness (up to $3.8 \cdot 10^6 \text{ M}^{-1} \text{ cm}^{-1}$) of the nano-hybrids and their bathochromic shift (>1250 nm), allowed fluorescence images at depths reaching 7 mm, which confirmed the large potential of these NPs for advanced NIR-II imaging.

2. Results and Discussion

2.1. Encapsulation

We used nanoprecipitation to assemble polymer NPs loaded with AuNCs, which is a particularly attractive approach due to its simplicity and tunability.^[23] In nanoprecipitation, both polymer and load are dissolved in a water miscible solvent, here acetonitrile, and the resulting solution is added to an aqueous phase (**Figure 1**). Mixing and interdiffusion of the organic and aqueous phase lead to a mixture, in which the polymer and the load are not soluble anymore, creating supersaturation, which is, in turn, the driving force for particle formation. Because particle formation in this case is a kinetically controlled process, it allows for trapping the load. Apart from the assembly conditions, the nature of the polymer can be used to optimize encapsulation. We chose poly(ethyl methacrylate) (PEMA) based polymers, as they have shown very good results for the encapsulation of hydrophobic fluorescent dye salts with high QYs.^[24] The polymers contained 5 or 10 mol% of COOH groups in order to control the size of the resulting NPs (**Figure 1**).^[25] On the side of the load, dodecanethiol (DDT) was chosen as ligand during cluster formation following a well-established protocol^[26] in order to achieve a high hydrophobicity of the resulting AuNCs with a good control of the NC size. The obtained products after purification had a diameter of $1.84 \pm 0.34 \text{ nm}$, as determined by HR-TEM (**Figure S1**, Supporting Information).^[22a] The absorbance profile of our AuNCs, notably with the band at $\approx 700 \text{ nm}$, is characteristic of the presence of Au₂₅ NC species.^[27] Together, these results indicate that the obtained product is composed of a majority of Au₂₅DDT₁₈ clusters, though a certain distribution of cluster sizes is certainly present.

Dynamic light scattering (DLS) showed increasing sizes of the obtained NPs with increasing AuNC loading (**Figure 2A**). Polymers with 10% of charged groups gave NPs roughly half the size of those bearing 5%, and the sizes of the highest loaded NPs had hydrodynamic diameters of 41 ± 7 and $68 \pm 6 \text{ nm}$, respectively. Certain NPs based on the polymers bearing 5% charged groups were further investigated by TEM imaging (**Figure 2B**), showing monomodal size distribution and a slightly smaller diameter ($60 \pm 13 \text{ nm}$) compared to DLS. The latter can be attributed to the fact that DLS measures the

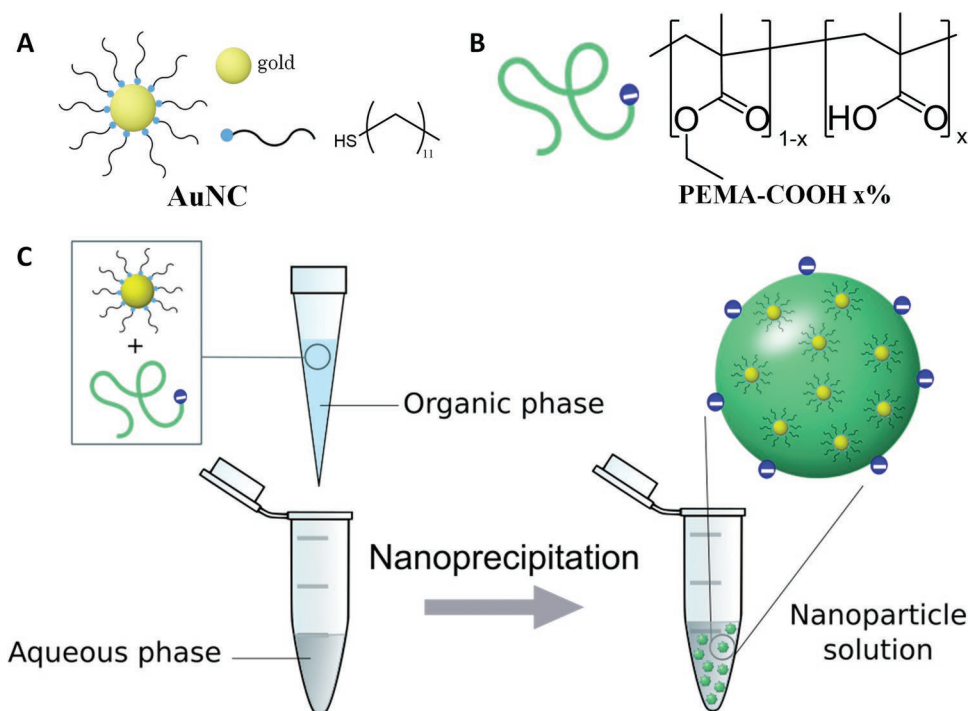


Figure 1. A) Structure and representation of gold nanoclusters stabilized by dodecanethiol (AuNC). B) Structure and representation of the polymer. C) Principle of NP synthesis through nanoprecipitation.

hydrodynamic diameter that is usually larger than the TEM hard sphere diameter. TEM images also showed an increasing contrast with increasing AuNC loading (in the absence of contrast agent, Figure S2, Supporting Information). High-resolution cryo-TEM images further revealed the presence of small dots with sizes ≤ 2 nm, corresponding to the size of the AuNCs, whose numbers per particle increased with loading (Figure 2C). No obvious organization, e.g., clustering that would be expected to yield zones of much higher contrast, was observed when examining a large number of nanohybrids at different loadings (Figure 2C and Figure S2, Supporting Information). ICP-MS analysis of NPs, purified through centrifugational filtration to evacuate all non-encapsulated materials, indicated a linear increase of the amount of gold with loading and an

excellent agreement with the calculated expected gold content (Figure 2D). Together, these results indicated a practically quantitative encapsulation of the AuNCs in the polymer NPs.

Calculations, based on the size of the NPs, as obtained from TEM, and the mass concentration of clusters inside the NP, were used to approximate the number of clusters encapsulated in one NP. For this, we assumed complete encapsulation of the AuNCs in the polymer NPs (see above) and estimated a mean density of the NPs based on the densities of the polymer material and gold and their weight fractions (see Experimental Section for details on the calculations). For NPs loaded with 9 wt%, we estimated that around 100 AuNCs were encapsulated in one NP, this number growing strongly with the loading and reaching almost 14000 for the highest loading (50 wt%, Table 1).

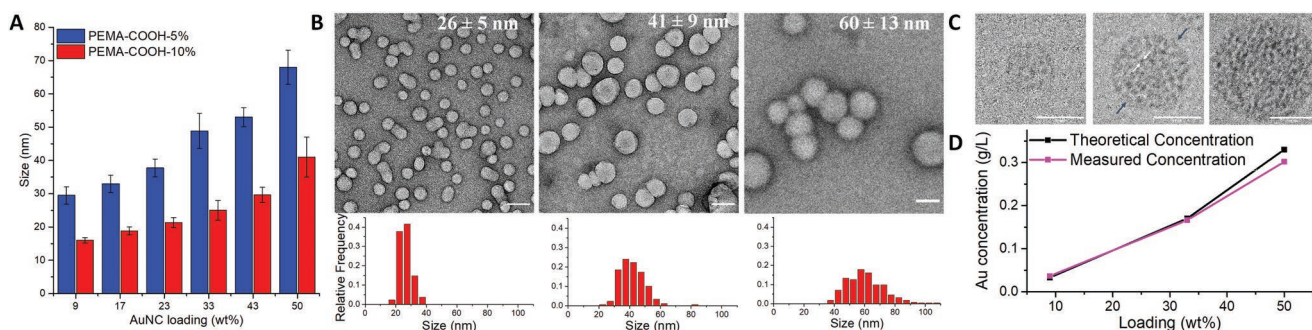


Figure 2. A) NP size (hydrodynamic diameter) measured by DLS for two polymers. B) TEM images of NPs (from left to right) for 9, 33 and 50 wt% of AuNC loading and their size (hard sphere diameter) distributions. Scale bars: 50 nm. C) Cryo-TEM images of NPs (from left to right) for 9, 33 and 50 wt% of AuNC. Dark arrows show NP and white arrows show AuNC (≈ 2 nm). Scale bars: 20 nm. D) Gold concentration inside NPs as measured by ICP-MS compared to calculated concentration.

Table 1. Properties of AuNC-loaded polymer NPs.

| Loading AuDDT [%] | Size in DLS [nm] | Size in TEM [nm] ^{a)} | Number of AuNCs per NP ^{b)} | AuNC distance inside NPs ^{c)} [nm] | $\epsilon_{\text{NP}} 730 \text{ nm}$ [$\text{M}^{-1} \text{cm}^{-1}$] ^{d)} | $\epsilon_{\text{NP}} 405 \text{ nm}$ [$\text{M}^{-1} \text{cm}^{-1}$] ^{d)} | Quantum yield [%] ^{e)} | Brightness ($\lambda_{\text{ex}} 730 \text{ nm}$) [$\text{M}^{-1} \text{cm}^{-1}$] ^{f)} | Brightness ($\lambda_{\text{ex}} 405 \text{ nm}$) [$\text{M}^{-1} \text{cm}^{-1}$] ^{f)} |
|-------------------|------------------|--------------------------------|--------------------------------------|---|--|--|---------------------------------|--|--|
| 9 | 30 ± 3 | 26 ± 5 | 120 | 2.6 | 1.7 × 10 ⁶ | 8.77 × 10 ⁶ | 1.3 | 2.3 × 10 ⁴ | 1.1 × 10 ⁵ |
| 33 | 49 ± 6 | 41 ± 9 | 2300 | 1.4 | 3.3 × 10 ⁷ | 1.68 × 10 ⁸ | 0.6 | 2.0 × 10 ⁵ | 9.9 × 10 ⁵ |
| 50 | 68 ± 6 | 60 ± 13 | 14 000 | 1.1 | 2.0 × 10 ⁸ | 1.03 × 10 ⁹ | 0.4 | 7.6 × 10 ⁵ | 3.8 × 10 ⁶ |

^{a)}Average size of > 200 NPs ± width at half maximum; ^{b)}Estimated based on Equation (3); ^{c)}Estimated based on Equation (4); ^{d)}Calculated according to $\epsilon_{\text{NP}} = \text{Number of AuNCs} \times \epsilon_{\text{AuNC}}$; ^{e)}Measured using IR1061 as reference; ^{f)}Calculated according to brightness = $\epsilon_{\text{NP}} \times \text{QY}$.

These values are in qualitative agreement with the obtained high resolution cryo-TEM images, though the latter do not allow a quantitative assessment of the number of AuNCs. Once we knew the cluster concentration inside a NP, we could estimate the average distance between clusters. This distance (being highly linked to the loading) was approximately half between the lowest and the highest loading (Table 1). At 50 wt% loading, it reached an average center to center distance of about 2 nm (assuming a cubic lattice) and an average nearest neighbor distance of 1.1 nm (assuming an isotropic random distribution).^[28]

2.2. Photophysical Properties

Polymer NPs loaded with AuNCs showed broad absorption spectra, ranging from the UV region to the NIR with two main peaks around 416 and 708 nm (Figure 3A), very similar to the spectrum of the clusters in organic solvent. While the absorbance increased linearly with loading, the shape of the spectra remained practically unchanged. Based on the calculated number of AuNCs per NP, and the extinction coefficient of the AuNCs of around 14000 $\text{M}^{-1} \text{cm}^{-1}$ at 730 nm (based on independent absorption measurements), and a five times higher value at 405 nm, the particle extinction coefficient at the two major absorption wavelengths reached values of circa $1 \times 10^9 \text{ M}^{-1} \text{cm}^{-1}$ (at 405 nm) and $2 \times 10^8 \text{ M}^{-1} \text{cm}^{-1}$ (at 730 nm). We also measured PL excitation spectra, which fitted very well to the absorption spectra and confirmed that the absorption spectra did not contain significant amounts of scattering (Figure S3, Supporting Information).

We further investigated the PL properties linked to these two peaks, by exciting respectively with a 405 nm and a 730 nm laser (Figure S4, Supporting Information). For both excitation wavelengths, the spectroscopic properties revealed to be similar, apart from the PL intensity, which was directly linked to the difference of absorbance between the two regions. Here, we focus on the results obtained with excitation at 730 nm, as this wavelength is better suited for in vivo imaging.

When studying the photophysical properties in the NIR-II, the influence of solvents has to be considered. Indeed, H₂O has various absorption peaks in the emission range of the NPs (Figure S5A, Supporting Information), which are absent for D₂O. Thus, we compared particles prepared in H₂O and D₂O. Comparison of the absolute PL emission of NPs (Figure 3B, inset) revealed that the shape of the PL emission spectrum changes between the two conditions, in particular with a decrease of the measured intensity in H₂O in the regions 930–1050 and 1100–1250 nm, corresponding to the absorption of water (Figure S5A, Supporting Information). On the other hand, we observed little difference between the maximum intensity of NPs prepared in the two aqueous media, suggesting that the clusters are well trapped inside the polymer matrix and have limited contact with water. Together these results indicated that the differences in the PL spectra stem mainly from the absorption of the emitted PL by H₂O, and not from interactions of H₂O with the encapsulated AuNCs. The same results were obtained for NPs prepared in D₂O and subsequently transferred to H₂O, indicating that preparation in D₂O did not alter the particles themselves. In order to study the properties

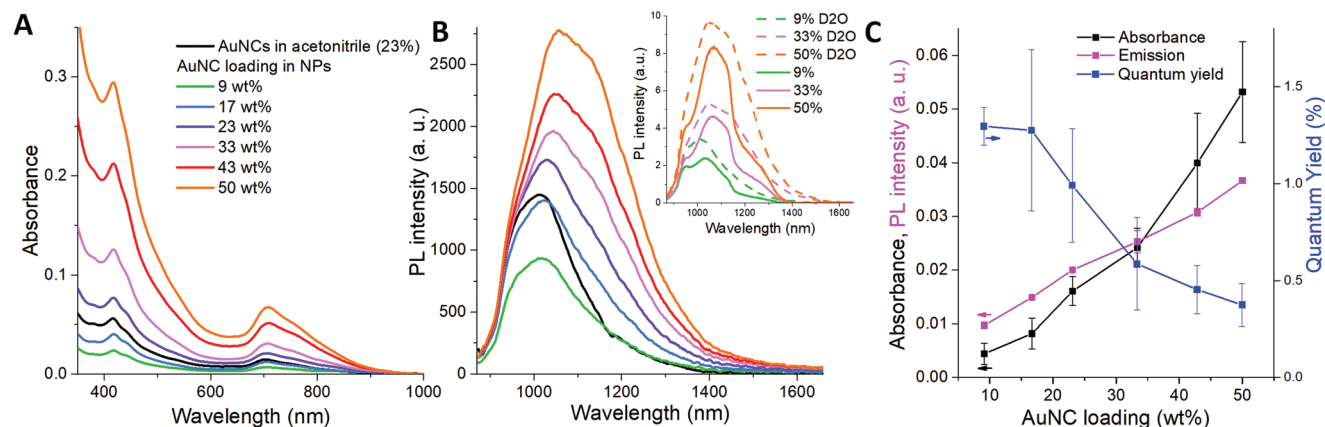


Figure 3. A) Absorbance and B) PL spectra of PEMA-COOH 5% NPs loaded with different amounts of AuNCs ($\lambda_{\text{exc.}} 730 \text{ nm}$). Inset of (B): Comparison of PL spectra in deuterated and nondeuterated media. C) Evolution of absorbance, PL intensity, and QY with loading.

of NPs without the solvent bias, all the following experiments were realized in deuterated water.

PL spectra of the AuNC loaded NPs showed a broad PL emission starting around 850 nm and reaching up to 1500 nm, achieving the objective of synthesizing NIR-II-emitting nanohybrids. The absolute emission intensity of the NPs increased continuously with AuNC loading (Figure 3B). To further evaluate the PL efficiency of our NPs, we measured the QYs for different AuNC loadings using the dye IR1061 as reference^[29] (Figure 3C). The free AuNCs in organic solution (acetonitrile) had a QY of 1%, in good agreement with previously measured QY values.^[13a] At low loadings of the AuNCs in the nanohybrids, the QYs were of the order of 1.3%, and they decreased with increasing loading to attain 0.4% at the highest loading, suggesting an ACQ-like phenomenon.^[30] Owing to the strongly increasing absorbance with increasing loading, the absolute PL intensity of NPs still increased even with the highest AuNCs content (Figure 3C), showing that the increasing number of clusters inside NPs significantly compensated the decrease in QY. The nanohybrid brightness can be estimated by multiplying the QY and the per-particle extinction coefficient. The elevated number of nanoclusters per nanohybrid at high loadings (up to 14000) resulted in per-particle brightness values of up to $3.8 \times 10^6 \text{ M}^{-1} \text{ cm}^{-1}$ and $7.6 \times 10^5 \text{ M}^{-1} \text{ cm}^{-1}$ for excitation at 405 nm and 730 nm, respectively. These values can be compared to those of other NIR-II contrast agents (Table 2): Typical NIR-II dyes, such as ICG or IR-E1050, have a brightness (in water) of the order of a few $10 \text{ M}^{-1} \text{ cm}^{-1}$,^[31] which is also the order of magnitude for chromophores specifically developed for use in blood.^[32] Somewhat higher brightness values are obtained for nanostructures, such as gold nanorods ($1200 \text{ M}^{-1} \text{ cm}^{-1}$),^[33] organic NPs based on chromophores undergoing AIE ($27000 \text{ M}^{-1} \text{ cm}^{-1}$),^[34] or QDs (e.g., $12000 \text{ M}^{-1} \text{ cm}^{-1}$).^[35] Thus, our nanohybrids are four orders of magnitude brighter than dyes emitting in the same wavelength range, and one to two orders of magnitude brighter than typical NIR-II emitting NPs.

To further study the influence of AuNC loading on our nanohybrids, the PL spectra were normalized (Figure S5B, Supporting Information), revealing that an increase in the AuNC concentration induced a shift in the PL toward longer wavelengths. For a better understanding of this evolution, we performed deconvolutions of the observed emission spectra (Figure 4). For simplicity, we chose to decompose the spectra into different Gaussian curves. The best fitting results were obtained for four Gaussians with maximum intensities at 947,

1010, 1120, and 1300 nm, respectively (Figure 4B, inset). This model was then applied to the spectra of NPs loaded with different AuNC concentrations and the absolute intensities of each peak were compared. In Figure 4A, two trends emerge from a comparison of the peaks: at lower wavelength (947 and 1010 nm), the absolute PL intensity remained nearly constant, independent of the AuNC concentration. On the contrary, absolute PL intensities of the two longer wavelength peaks (1120 and 1300 nm) increased with increasing AuNC concentrations. The resulting relative decrease/increase of lower/higher wavelength intensities was found for both 730 nm and 405 nm excitation (Figure S5C, Supporting Information).

Taking into account that the absorption also increases with increasing loading, a comparison of the absolute PL intensities of the different peaks can be misleading. Therefore, similar to the global PL analysis, we calculated the ratio of each PL peak intensity and its corresponding absorbance value (Figure 4B). As expected, (cf. QY in Figure 3C), all ratio values decreased with increased loading. However, the decrease was significantly less strong for the longer wavelength peaks. This suggests that the PL at longer wavelengths is less sensitive to an ACQ-type quenching behavior.

Through variation of the fraction of charged groups on the polymers used for nanoprecipitation, it was possible to obtain nanohybrids with different sizes but the same loading of AuNCs, in terms of wt%. (Figure 2A). PL measurements on nanohybrids with 33 wt% AuNC loading and sizes of 49 and 25 nm, respectively, showed that the overall PL was about 15% higher in case of the bigger sizes (Figure S6, Supporting Information). This difference mainly stems from a higher emission at the shorter wavelengths (950 and 1010 nm).

Considering that the inter-AuNCs distances within the NPs decrease with increased loading, we expected that the AuNC interactions would increase at the same time. Whereas the decrease of QY with increasing loading (Figure 3C) provided first important evidence for such stronger interactions, PL decay kinetics can potentially reveal more details. Because the steady-state spectroscopy results showed that the longer PL emission wavelengths were less influenced by AuNC concentration quenching (cf. Figure 4), we measured PL decays at 950 and 1050 nm for the short wavelength range and at 1200 nm for the long wavelength range. The wavelength of 1200 nm was chosen because it is significantly separated from the short wavelength peaks and still provides sufficient PL intensity for kinetic analysis. Different AuNC PL studies suggested that excitation at

Table 2. Properties of some NIR-II contrast agents in water.

| Contrast agent | Type | $\lambda_{\text{exc.}}$ [nm] | $\lambda_{\text{em.}}$ [nm] | ϵ [$\text{M}^{-1} \text{ cm}^{-1}$] | QY ^{a)} [%] | Brightness [$\text{M}^{-1} \text{ cm}^{-1}$] ^{d)} | Refs. |
|-------------------------|---------------|------------------------------|-----------------------------|--|----------------------|--|---------|
| ICG | dye | 785 | 1000–1300 | 1.5×10^5 | 0.9 | 6.5×10^1 | [31] |
| IR-E1050 | dye | 785 | 1000–1300 | 0.8×10^4 | 0.2 | 1.0×10^1 | [31] |
| LZ-1105 | dye | 1021 | 1060 | 1.08×10^5 | 0.06 | 6.5×10^1 | [32] |
| Gold nanorods | nanorods | 680 | 990 | 1.5×10^4 | 8 | 1.2×10^3 | [33] |
| TTQP | AIE based NPs | 683 | 1078 | 3.29×10^4 | 8 | 2.7×10^4 | [34] |
| Ag ₂ Se QDs | quantum dots | 800-930 | 1000 | 5.5×10^4 | 23 ^{b)} | 1.2×10^4 | [35a] |
| AuNC loaded polymer NPs | nanohybrids | 730 | 900–1400 | 2.0×10^8 | 0.4 | 7.6×10^5 | Current |

^{a)}In water, where not noted otherwise; ^{b)}in C_2Cl_4 ; ^{c)}calculated according to brightness = $\epsilon \times \text{QY}$.

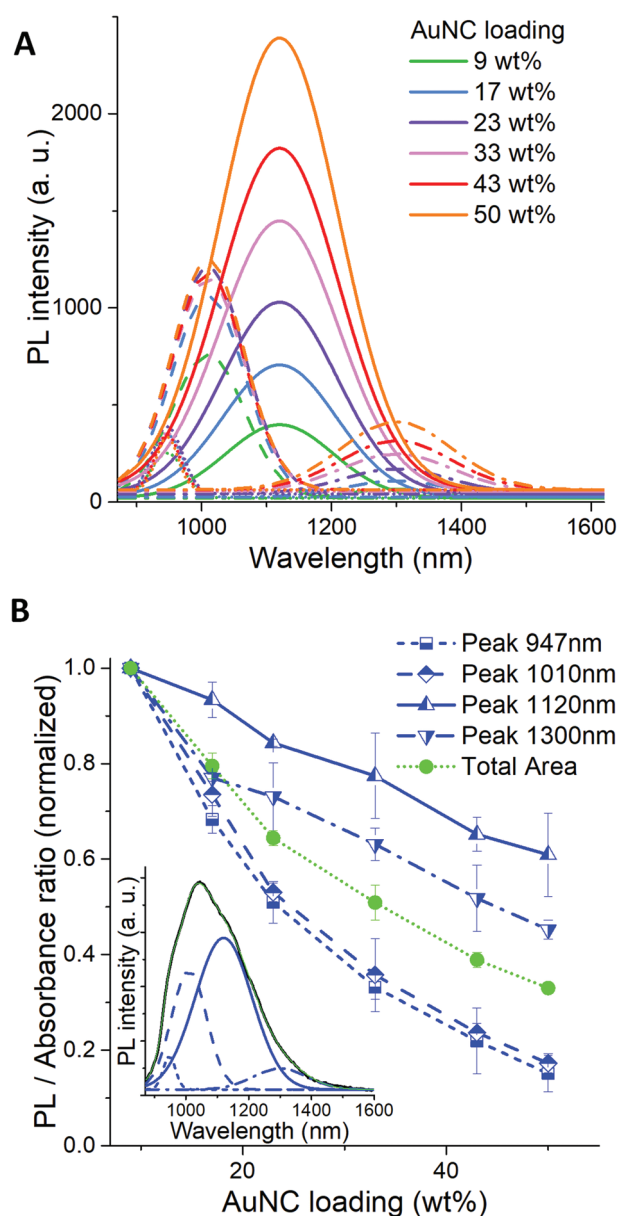


Figure 4. A) Gaussian peak fit for NPs with different loadings. B) Ratio between peak area and absorbance, normalized to the value at 9 wt% for comparison between the different peaks. Inset: Representation of the deconvolution of the PL emission spectrum of NPs, measured spectrum in black, fitted spectrum in green (black and green spectra are almost completely superimposed), result of deconvolution in blue.

the distinct absorption peaks resulted in preferential PL from either the AuNC core (700 nm excitation) or from the AuNC surface via ligand–metal interactions (400 nm excitation).^[27a,36] Thus, we investigated the PL kinetics using two different excitation lasers with wavelengths of 404 and 675 nm.

The multiexponential PL decays of AuNC loaded polymer NPs (Figure 5, top) clearly show different AuNC concentration-dependent behaviors for the different emission wavelengths. Whereas 950 nm emission presented a strongly pronounced longer decay time component, 1200 nm emission mainly showed faster decays, and the 1050 nm emission decay behavior

was in between the two others. The fitted PL decay times (Figure 5, center) and amplitude fractions (Figure 5, bottom) confirmed this trend. The 1200 nm emission was insensitive to the AuNC concentrations with two unchanged PL lifetimes and amplitude fractions, resulting in a stable average PL lifetime. Emission of pure AuNCs (data points at 0 wt%) was measured in ethanol and was very weak at 1200 nm, which explains the slightly lower decay time values. 950 and 1050 nm PL decays also showed two distinct PL lifetimes. However, whereas the shorter lifetime (τ_1 , black) was stable over the entire AuNC concentration range and corresponded very well to the one at 1200 nm, the longer decay time (τ_2 , red) was much higher at low AuNC loading and decreased toward the τ_2 value at 1200 nm with increasing AuNC loading. The long lifetime component was also significantly stronger for the 950 nm decay compared to 1050 nm, which showed that the influence of AuNC loading was stronger the shorter the emission wavelength. This trend is also visible in the amplitude-averaged PL lifetimes (blue data points in Figure 5, center). These results are in agreement with the steady-state spectroscopy, which showed that the redshift of the AuNC NPs with increasing AuNC concentration was mainly caused by a stronger PL decrease at shorter wavelengths (cf. Figure 4B).

Another interesting point concerns high AuNC loading (50 wt%), for which the single and amplitude-averaged PL lifetimes are very similar for all emission wavelengths (Figure 5, center). This behavior can be interpreted by a decreasing distance between the AuNCs with increasing loading. The longer PL emission wavelengths (>1200 nm) showed a long (≈ 400 ns) and a short (≈ 100 ns) lifetime component, which did not change with AuNC loading (Figure 5, center right). Considering that the PL intensity at 1200 nm was very weak for AuNCs in solution (Figure 5, top right) and that it was quenched less than the shorter wavelength PL intensity with increased loading (cf. Figure 4B), the longer PL wavelengths can be attributed to strongly interacting AuNCs. The shorter PL emission wavelengths (<1200 nm) showed a relatively strong long (>1 μ s) decay component together with a relatively weak short (≈ 100 ns) component (Figure 5, center left). The very long decay component is longest and strongest for AuNCs in solution (Figure 5, left). The higher the AuNC loading, the stronger it is quenched, until reaching the value of ≈ 400 ns, which presents the one of the strongly interacting AuNCs at 1200 nm. Therefore, the shorter wavelengths mainly present non-interacting or weakly interacting AuNCs, whose fraction strongly decreases with increasing loading due to shorter inter-AuNC distances within the NPs. Both the differences of luminescence decays at short (950 and 1050 nm) and long (1200 nm) emission wavelengths for lower AuNC loading (<50 wt%) and the red shift of the PL with increasing AuNC concentration (Figure 3B) can therefore be attributed to increasing AuNC interactions (closer inter-AuNC distances) that favor longer wavelength over shorter wavelength PL emission.

Intriguingly, only the longer PL lifetime component was influenced by AuNC loading, whereas the shorter component was more or less constant (≈ 100 ns) for all emission wavelengths and AuNC loadings (Figure 5, center). This specific property of the AuNC NPs can be explained by the different origins of AuNC emission. Taking into account the very weak

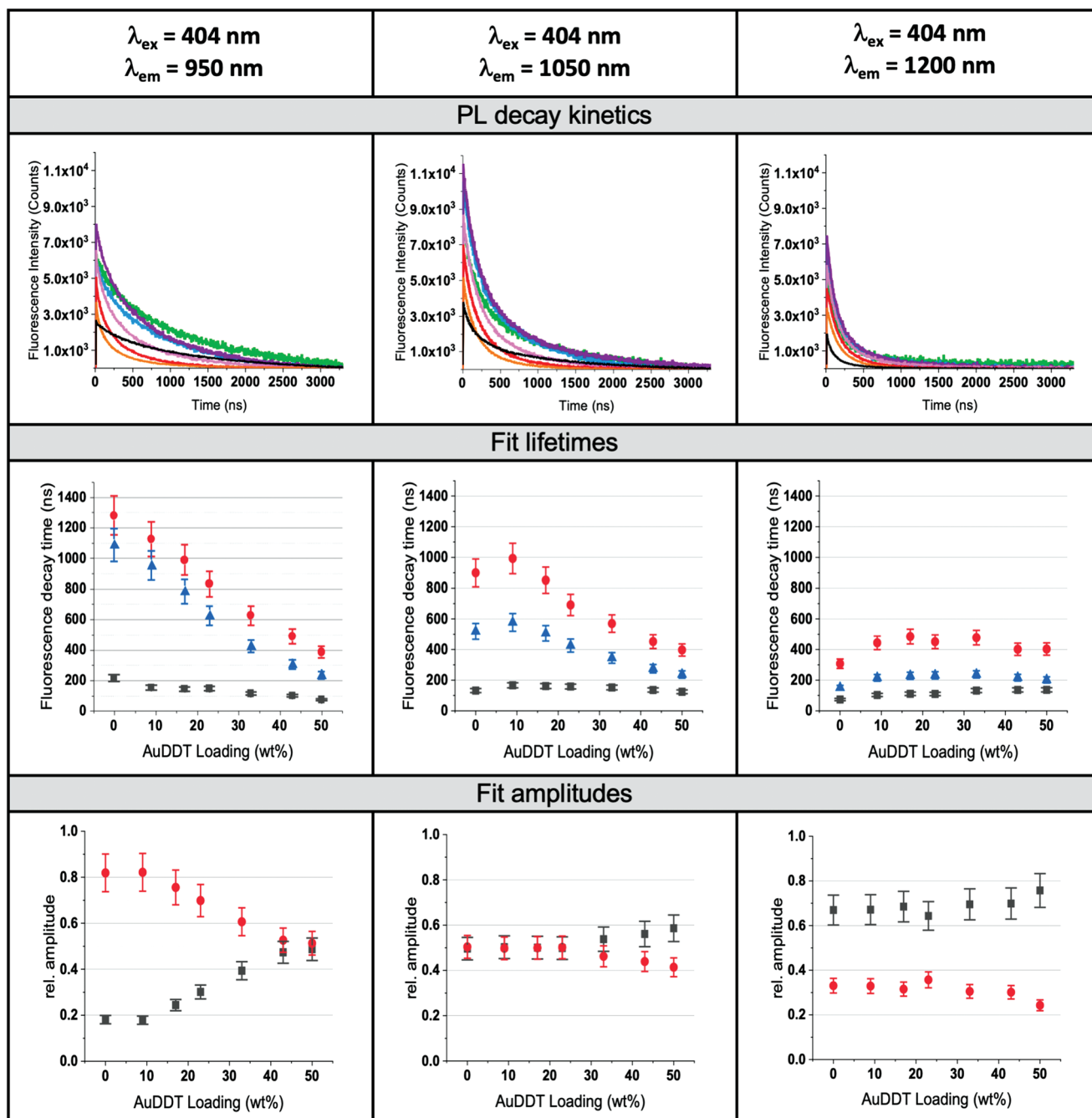


Figure 5. Intensity-comparable (the curves from each graph were normalized for similar excitation intensity and similar absorption and background was subtracted) PL decays (top row—brown: AuNCs; orange: 50 wt%, red: 43 wt%; magenta: 33 wt%; purple: 23 wt%; blue: 17 wt%; green: 9 wt%), fit PL lifetimes (black: τ_1 ; red: τ_2 ; blue: τ_3), and fit amplitude fractions (black: x_1 ; red: x_2) of AuNCs (in ethanol) and AuNC-NPs (AuDDT in D₂O) for excitation (λ_{ex}) at 404 nm and emission (λ_{em}) at different wavelengths (950, 1050, and 1200 nm). 0 wt% loading corresponds to AuNCs in ethanol. Raw PL decay curves and the different normalization steps are shown in Figure S7 (Supporting Information).

spectral overlap of AuNC emission and absorption, F rster resonance energy transfer (homo-FRET—cf. incl. Figure S8, Supporting Information, for estimation of F rster distances) would require very short donor–acceptor distances (≈ 1 to 2 nm). With a AuNC radius of approximately 1 nm, FRET from AuNC surfaces would be clearly favored over FRET from AuNC cores. At very close distances, other energy transfer mechanisms that

require orbital overlap, such as Dexter or charge transfer, may become even more probable than FRET,^[37] and these would only occur between the AuNC surfaces. Thus, the constant short PL lifetime component mainly represents PL originating from the AuNC core, whereas the quenched long component represents the ligand-metal charge-transfer related PL originating from the AuNC surface.

Interestingly, excitation at 675 nm (instead of 404 nm) resulted in very similar PL decay kinetics, including PL lifetimes and amplitude fractions (Figures S9 and S10, Supporting Information). These findings show that there is no difference of exciting the AuNCs in the short or long wavelength absorption band and that there is no excitation-wavelength dependent emission of the AuNC core or ligand-metal-surface states. Although this result is contradictory to previous studies,^[27a,38] we note that the size distribution and the nature of the ligand often have a significant impact on PL emission properties notably in the near-infrared region. Indeed, in our case we did not observe AIE behavior, as was previously described for aggregation of AuGSH NCs.^[39] A possible reason might be the poorly efficient ligand–metal and ligand–metal–metal charge transfer of the aliphatic DDT ligands here, compared to electrophilic GSH ligands.^[27a,40] While our results provide a new perspective on interaction-dependent AuNC emission behavior, more studies with detailed and comprehensive AuNC PL characterization of many different types of AuNCs will be necessary to fully understand AuNC PL.

2.3. NIR-II Imaging on Tissue Models

To evaluate the suitability of our nanohybrids for NIR-II imaging in terms of photophysical properties, we measured their PL with a NIR-II camera and at different tissue depths, using an appropriate phantom model system. In the first step, we

measured the PL intensities of concentrated nanohybrid solutions with different AuNC loadings from 0 to 50 wt% selecting different sub-optical windows in the NIR-II (Figure 6A). Under NIR excitation ($\lambda = 808$ nm—which is not ideal for AuNC absorption but better suited for tissue penetration compared to excitation in the visible wavelength region), nanohybrid solutions ($300 \mu\text{g mL}^{-1}$) showed an increasing NIR-II signal with increasing AuNC loading and could be detected even in the NIR-IIb region between 1500 and 1700 nm for the highest loading of 50 wt% (Figure 6B). This trend remained valid for more diluted samples (Figure S11, Supporting Information). Quantification of the PL signal from AuNC loaded NPs in the different sub-optical windows (Figure 6C) clearly indicated that most of the PL was emitted below 1319 nm with a linear increase with AuNC loading. However, SNR remained higher than 3 for NPs loaded with 33 and 50 wt% of AuNCs even above 1400 nm for concentrated (Figure 6C) and diluted samples (Figure S11, Supporting Information). This suggests that highly loaded nanohybrids may even be applicable as *in vivo* contrast agents in the NIR-IIb region.

In the next step, we wanted to quantify how the loading of the nanohybrids with AuNCs influences the depth and the resolution that can be reached, e.g., for imaging blood vessels *in vivo*. Instead of sacrificing animals, a much better approach for characterizing tissue penetration depth and spatial resolution for blood vessel imaging is the use of tissue mimicking phantom models composed of nanohybrid-filled capillaries placed at different depths in a 1% intralipid solution (cf. Experimental

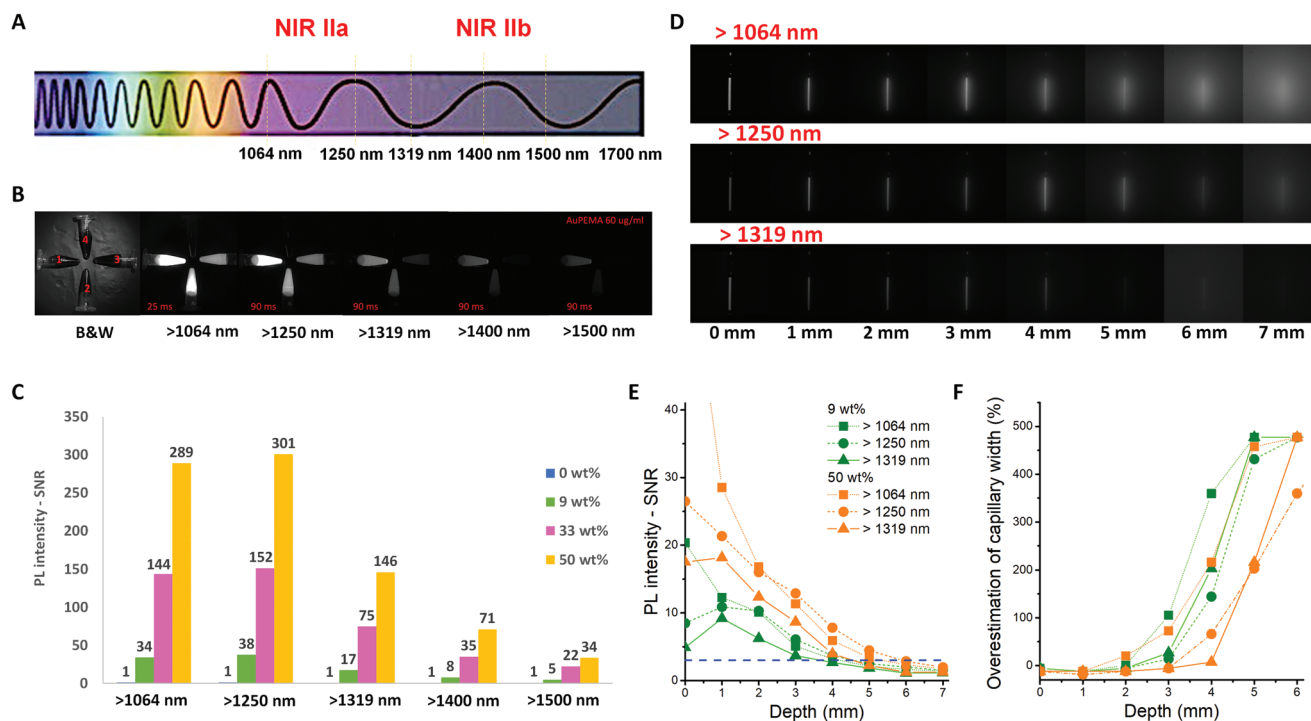


Figure 6. NIR-II imaging of Au-PEMA solutions in tubes and capillaries. A) Suboptical NIR-II window. B) NIR-II images of plastic tubes filled with AuNC loaded PEMA NPs ($300 \mu\text{g mL}^{-1}$) at 0 wt% (4), 9 wt% (3), 33 wt% (2), and 50 wt% (1) AuNC loading using different long pass (LP) filters. C) PL intensity expressed in SNR of AuNC NP solution ($300 \mu\text{g mL}^{-1}$) at different AuNC loading. D) PL images of capillaries filled with AuNC NPs (50 wt% of AuNC) at different depths in intralipid solution (1%) using LP1064 nm, LP1250 nm, and LP1319 nm. E) PL intensity profiles of AuNC NPs in capillaries at different intralipid heights using different LP filters. F) Overestimation of the capillary width (%) at different intralipid heights using different LP filters. SNR threshold = 3. λ_{exc} 808 nm.

Section and Figure S12, Supporting Information).^[41] Indeed, this model allows simulating the imaging of blood vessels at different depths below the skin, with the possibility to precisely position the capillaries and to evaluate and compare the performance of the different contrast nanoagents. Two of the most important parameters for imaging are the sensitivity of detection and the overestimation of the widths of capillaries, which we determined as a function of the tissue phantom depth and the AuNC loading. As expected from the wavelength-dependent PL intensities (Figure 6C) and the intralipid-induced absorption and scattering, the PL intensities originating from the capillaries decreased with increasing emission wavelengths and higher depths (Figure 6D). Although increasing tissue thicknesses also resulted in a more scattered (blurred) image of the capillaries (Figure 6D from left to right), increasing PL wavelengths clearly reduced the scattering (Figure 6D from top to bottom).

Quantification of images measured with nanohybrids at different AuNC loading and in different sub-optical windows are presented in Figure 6E,F. A SNR of 3 was used as detection limit for evaluating the detection sensitivity.^[42] While there was no significant benefit of selecting a sub-optical window at wavelengths beyond 1250 nm (due to the decreasing PL intensities), there was a clear improvement of the sensitivity when using NPs with the highest AuNC loading. For instance, NPs loaded with 50 wt% of AuNCs could be detected above the defined SNR threshold at 5 mm depth using a >1250 nm long pass filter with a SNR of 5, whereas lower AuNC loadings did not allow to reach sufficiently high SNR at this depth (Figure 6E and Figure S13, Supporting Information). The overestimation of the capillary width directly provides a measure of the accomplishable spatial resolution. In general, placing fluorescent objects in diffuse environments leads to a strong scattering enhancement with a rapid overestimation of their real size.^[42] We plotted the percentage of overestimation of the capillary width as a function of the tissue phantom depths as extracted from the NIR-II images (Figure 6F and Figures S14–S17, Supporting Information). Reduced scattering using both longer wavelengths and higher AuNC loading could be clearly observed. Selecting the >1319 nm wavelength range and 50 wt% loading of AuNCs it was possible to detect capillaries with a good spatial resolution, which corresponded to less than 20% of overestimation, at 4 mm depth in intralipids.

3. Conclusion

Here, we assembled a first series of polymer NPs loaded with high amounts of gold nanoclusters emitting in the NIR-II spectral region. Their efficient encapsulation within the polymer matrix allowed obtaining nanoparticles of about 60 nm containing over 10 000 clusters each. Even though a slight ACQ effect was observed, relatively good quantum yields could be obtained even at very high AuNC loadings. In this way, an exceptional particle PL brightness for the NIR-II region in the order of $4 \times 10^6 \text{ M}^{-1} \text{ cm}^{-1}$ could be reached, which places our nanohybrids among the brightest NIR-II emitters. The high AuNC concentrations inside the particles further gave the possibility to study the PL properties at very small intercluster dis-

tances. Surprisingly, a bathochromic shift of the PL emission with loading was observed. Spectral deconvolution together with time-resolved PL measurements related different sensitivities of different emission modes to interactions between clusters: While emission from the Au core was little affected by the distance between clusters, emissions involving ligand–metal–surface states experience a relatively strong ACQ effect. In consequence, the PL maximum is shifted to longer wavelengths at higher loadings and thus further into the NIR II region. Our results stipulate that precisely engineering the distances and interactions of AuNCs can be a way of optimizing and tailoring their PL properties. The combination of very high PL brightness with a shift to longer emission wavelengths for the highest AuNC loadings resulted in significantly improved detection and resolution when using these nanohybrids in phantom models for in vivo blood vessel imaging. The combination of very high brightness, well-characterized PL behavior and excellent performance in tissue models, makes the nanohybrids developed here ideal candidates for advanced in vivo imaging as well as for further studies on the PL mechanisms of AuNCs. Detailed characterization concerning the biological response to the nanohybrids, their stability under biological conditions, and in vivo imaging studies will be investigated in forthcoming studies.

4. Experimental Section

Synthesis of Gold Nanoclusters (AuNCs): Gold nanoclusters stabilized by dodecanethiol (DDT), called here AuNCs, were prepared as described elsewhere.^[26] Briefly, 46.4 mg (93.75 μmol) AuClPP₃ were dispersed in ethanol followed by addition of 81.5 mg (0.94 μmol) *tert*-butylamine-borane and fast stirring for 45 min. The solution changed from orange-red to black color after 5 min. Then 12 μL of DDT was added and the mixture was left to stir for another 3 h. The dark solution was then filtered 3 times with filters at 3 kDa molecular weight cut-off to remove unreactive species and kept refrigerated.

Preparation of NPs: Polyethylmethacrylate (PEMA) bearing 5 or 10 mol% of methacrylic acid was synthesized through free radical polymerization as described previously.^[24a,43] Stock solutions of PEMA were prepared at a concentration of 10 g L⁻¹ in acetonitrile. These solutions were diluted to 2 g L⁻¹ in acetonitrile, with 9 to 50 wt% of AuNCs (relative to the total mass of polymer and AuNC). These solutions were quickly added to a ninefold volume excess of phosphate buffer (20 $\times 10^{-3}$ M, pH 7.4) under shaking (Thermomixer comfort, Eppendorf, 1050 rpm at 21 $^{\circ}\text{C}$), followed by further dilution to the desired concentration.

Dynamic Light Scattering (DLS) and ζ -Potential: The size and ζ -potential of the mixed polymer NPs were measured on a Zetasizer Nano series ZSP (Malvern Instruments). For size determination, each sample was measured 10 times with a run length of 10 s each. Volume-averaged values, determined by the Zetasizer software based on Mie theory, were used. Mean values give the average over at least three independent preparations, error bars correspond to the standard error of the mean. For ζ -potential determination three successive measurements combining electrophoretic mobility and laser Doppler velocimetry with >10 runs each were carried out with an applied potential of ± 150 V.

Transmission Electron Microscopy (TEM): Solutions of NPs (5 μL) were deposited onto carbon-coated copper–rhodium electron microscopy grids following amyl amine glow discharge. They were then treated for 20 s with a 2% uranyl acetate solution for staining. The obtained grids were observed using a Tecnai F20 Twin transmission electron microscope (FEI Eindhoven Holland) operating at a voltage of 200 kV. Images (2048 pixels \times 2048 pixels) were recorded using a US1000 camera (Gatan) and analyzed using the Fiji software. At least 200 particles per condition were analyzed.

Cryo-TEM: 3 μL of sample was deposited onto freshly plasma-cleaned (Fishione 1070) 300 mesh Quantifoil R2/2 grids (Quantifoil Micro Tools GmbH, Jena, Germany) and the grids were plunge-frozen using a Vitrobot Mark IV (FEI) with 95% chamber humidity at 15 $^{\circ}\text{C}$ (blot force 5, blotting time 2 s). CryoEM imaging was performed on Glacios (FEI) microscopes operated at 200 keV acceleration voltage and equipped with a K2 Summit camera (Gatan, Inc., Pleasanton, CA) using SerialEM software. All images were acquired at a target defocus of 1.5 μm with a dose of $\approx 40\text{ e}^{-}\text{Å}^{-2}$ in super-resolution mode at a nominal magnification of 45000 \times , corresponding to a pixel size of 0.90 Å .

Estimation of the Number of AuNCs per NP: The volume of one NP was calculated based on the mean NP diameter determined by TEM. The NP mass (m_{NP}) was then determined using a mean density based on the loading of AuNCs inside the particle (L) and the densities of Au (ρ_{AuNC}) and of the polymer (ρ_{PEMA}):

$$\rho_{\text{NP}} = \frac{1}{\frac{1-L}{\rho_{\text{PEMA}}} + \frac{L}{\rho_{\text{AuNC}}}} \quad (1)$$

The mass of AuNCs per particle (m_{AuNC}) was calculated using:

$$m_{\text{AuNC}} = m_{\text{NP}} \times L \quad (2)$$

The number of AuNC per NP (N_{AuNC}) was calculated by taking into account the molar mass of the cluster ($M_{\text{AuNC}} = 5000\text{ g mol}^{-1}$ with respect to Au, with N_{A} the Avogadro constant):

$$N_{\text{AuNC}} = \frac{m_{\text{AuNC}} \times N_{\text{A}}}{M_{\text{AuNC}}} \quad (3)$$

Uncertainties on the obtained values originate from the size measurement and the used density of the polymer–AuNC nanohybrid, but are difficult to estimate.

Intercluster Distance: In the case of an isotropic random distribution, the average nearest neighbor distance can be estimated according to:^[28]

$$d = \frac{0.554}{\sqrt[3]{C}} \quad (4)$$

with C the concentration (number of AuNCs per volume) of AuNCs inside NPs.

Apart from the uncertainties related to the number of AuNCs per NP, the distribution of the clusters inside the NPs also influences the obtained values.

Spectroscopic Properties: Absorption spectra were recorded on a Cary 5000 Scan ultraviolet–visible spectrophotometer (Varian). PL spectra were recorded on a WP NIR1 spectrometer (Wasatch Photonics) using 405 or 730 nm lasers from LCC Oxxius as excitation sources. Excitation spectra were measured on a Fluorolog-3 (Horiba Instruments) equipped with a near-infrared detector. 0.1 mg mL^{-1} of the samples were loaded into capillary tubes to reduce the light path length and thus, the light scattering in the samples. The emission wavelength was fixed to 1050 nm and the excitation spectra were measured from 360 to 1000 nm. The excitation slit was set to 3 nm, whereas the emission slit was set to 8 nm. Raw excitation spectra were corrected by dividing the excitation signal by the corrected lamp signal (T1/R1c). An empty capillary tube was measured as the blank control. T1/R1c of the blank was subtracted from T1/R1c of the sample to obtain the final excitation spectra of the samples.

To compare peak ratios (R) of excitation and absorption spectra (measured on a Cary 60, Agilent Instruments, in quartz cuvettes with 0.5 cm path length) the average intensities from 404 to 406 nm were divided by the average intensities from 669 to 671 nm:

$$R = \frac{\text{avg.int.}(404 - 406\text{ nm})}{\text{avg.int.}(669 - 671\text{ nm})} = \frac{A}{B} \quad (5)$$

Errors were calculated by error propagation:

$$\Delta(R) = \sqrt{\left(\frac{a}{A}\right)^2 + \left(\frac{b}{B}\right)^2} \times R \quad (6)$$

where a is the standard deviation of A and b is the standard deviation of B .

Quantum Yields: QYs were determined from the absorbance values at the excitation wavelength ($A_{x,808\text{ nm}}$) and the integral over the whole emission range (F_x) using a simplified relative method with IR1061 in dichloromethane as reference (QY = 0.0041, absorbances below 0.1),^[29] according to the formula

$$QY_{\text{NP}} = QY_{\text{IR1061}} \frac{F_{\text{NP}} A_{\text{NP},808\text{ nm}} n_{\text{H}_2\text{O}}^2}{F_{\text{IR1061}} A_{\text{IR1061},808\text{ nm}} n_{\text{DCM}}^2} \quad (7)$$

where “NP” corresponds to solutions of the NPs in deuterated water, “IR1061” to the reference in dichloromethane (DCM), and n to the respective refractive indices of the solvents (1.33 for water and 1.42 for DCM).

Brightness: The brightness B is the product of the extinction coefficient of AuNC ϵ_{spe} , the number of AuNCs per NP (N_{AuNC}), and the QY of the NP (QY_{NP}):

$$B = N_{\text{AuNC}} \times \epsilon_{\text{AuNC}} \times QY_{\text{NP}} \quad (8)$$

The specific extinction coefficient ϵ_{spe} was determined through absorbance measurements with a solution of known concentration of AuNCs.

PL Lifetime Measurement: PL lifetimes were measured on a Fluorolog-3 with 400 μL of samples in quartz cuvettes with a 0.5 cm path length. PL decay curves were measured at three emission wavelengths, namely 950, 1050, and 1200 nm using two different picoseconds pulsed diode lasers from Edinburgh Instruments: 1) EPL 405 (Serial number: 083/405/11/11) with a pulse width of 56.3 ps and emission peak centered at 404.2 nm; 2) HPL 670 (Serial number: 010/670/04/21) with a pulse width of 104.4 ps and emission peak centered at 675.4 nm. The lasers were set at a repetition rate of 200 kHz (5 μs pulse period). When measuring with EPL 405 nm, the emission slit was set to 30 nm. When measuring with HPL 670, the emission slit was set to 58.8 nm (fully open) because the absorption in the 675 nm spectral region is at least 3 times lower than the one at 404 nm. In Datastation software (Horiba), time-correlated single-photon counting (TCSPC) was set for 3.34 ns per channel and 1000 channels. The measurement was set to end upon counting 20 000 photons as the maximum value. Decay curves were fit using FAST software (Edinburgh Instruments). The exponential components analysis routine was used to do the biexponential fitting of the curves. The fitting range was from channels 3 to 650 for measurements using EPL 405 and from channels 5 to 650 for measurements using HPL 670. Biexponential fitting (Equation (9)) was found sufficient for good fits of the decay curves.

$$I(t) = X_1 e^{-\frac{t}{\tau_1}} + X_2 e^{-\frac{t}{\tau_2}} + C \quad (9)$$

Relative amplitudes x_1 and x_2 and amplitude-averaged lifetimes $\langle \tau \rangle$ were calculated from the resulting exponential data as follows:

$$x_1 = \frac{X_1}{X_1 + X_2} \quad (10)$$

$$x_2 = \frac{X_2}{X_1 + X_2} \quad (11)$$

$$\tau = x_1 \tau_1 + x_2 \tau_2 \quad (12)$$

In these equations, X_1 and X_2 are amplitudes of the first and second lifetime components τ_1 and τ_2 , respectively, C is the background intensity, and $I(t)$ is the time-dependent PL intensity. Lifetime errors were estimated as 10% relative errors.

For an excitation-independent comparison of the decay curve intensities, the decay curves were normalized to a constant number of excitation pulses and to constant absorbance values of the sample. The pulse number is the product of the measurement runtime and the repetition rate of the laser (200 kHz). The average absorbance between 404 and 406 nm and 669 and 671 nm was normalized to the absorbance of the 9 wt% sample. The pulse numbers were normalized to the pulse number of the 9 wt% sample. The decay curves were then multiplied by the normalized number of pulses and divided by the normalized absorption at the wavelength of interest. The background (last intensity point of the decay curve) was then subtracted to receive background-corrected decay curves.

Inductively Coupled Plasma Mass Spectrometry (ICP-MS): Gold loading in polymeric NPs was determined using a quadrupole ICP-MS (Perkin Elmer NexION 2000, Waltham, MA, USA). Standard solutions were prepared in aqua regia 3% (v/v). ¹⁹⁷Au was measured and ¹⁰³Rh at 141 nmol L⁻¹ was used as internal standard. NP solutions were purified using 10 kDa centrifugal filters prior to ICP analysis. The theoretical gold concentrations were estimated based on the global polymer concentration and on the amount of AuNCs employed for particle assembly.

NIR-II imaging was performed using a Princeton camera 640ST (900–1700 nm) coupled with a laser excitation source at $\lambda=808$ nm (100 mW cm⁻²). A short-pass excitation filter was used at 1000 nm (Thorlabs) and a series of long-pass filters (LP) on the emission at 1064 nm (Semrock), 1250 nm (Thorlabs), 1319 nm (Semrock), 1400 nm (Thorlabs), 1500 nm (Thorlabs). A 50 mm lens with a numerical aperture of 1.4 (Navitar) was used to focus on the capillaries system.

Capillaries Imaging: Effect of scattering on the spatial resolution was estimated using a fine bore polythene tubing (OD = 0.96 mm/ID = 0.58 mm; Portex) filled with AuNC-loaded NPs and immersed in a 1% intralipid solution at increasing depths between 1 and 8 mm. Each condition was recorded through the 50 mm fixed focal length lens with exposure time from 10 ms to 2 s. Measurements were reproduced three times for each condition.

Data Analysis: Image analysis was performed using ImageJ software. Measurements of signal intensity were done in a defined region of interest (ROI) manually located on the capillary without intralipid and kept unchanged for all intralipid heights. The noise was measured at the edge of images in an area without a relevant signal. SNR was calculated as the mean signal intensity from the capillary divided by the noise. An arbitrary threshold value of 3 was fixed as a limit for SNR. Below this value, we considered that the signal from the capillary was not significant.

To evaluate scattering effect on each image, a cross-sectional intensity profile of the capillary was performed using the plot profile module of ImageJ software. The full width at half maximum (FWHM) evaluated by a fit of a Gaussian curve (Origin Pro 7 software) was obtained on each profile to describe the capillary width imaged by the camera for each condition. The FWHM or relative width obtained was compared with the real width of the capillary as a percentage defined as:

$$\% = \text{fitFWHM} / \text{constructor width} \times 100 \quad (13)$$

Supporting Information

Supporting Information is available from the Wiley Online Library or from the author.

Acknowledgements

The authors thank the French Agence Nationale de la Recherche (project LAPIN – ANR-20-CE09-0021-04), the FRC (Emerging Investigators grant), the Brain Pool program funded by the Ministry of Science and ICT through the National Research Foundation of Korea

(2021H1D3A2A0204958912), la ligue contre le cancer (R2104CC), Seoul National University, Universit  de Rouen Normandie, Normandie Universit , INSA Rouen, CNRS, European Regional Development Fund, Labex SynOrg (ANR-11-LABX-0029), Carnot Institute I2C, XL-Chem graduate school (ANR-18-EURE-0020 XL CHEM), and the Region Normandie for financial support. The authors also acknowledge the support and the use of resources of the French Infrastructure for Integrated Structural Biology FRISBI ANR-10-INBS-05 and of Instruct-ERIC and especially C. Crucifix for help with electron microscopy. X.L.G. thanks Benoit Chovelon for the ICP measurement.

Conflict of Interest

The authors declare no conflict of interest.

Data Availability Statement

The data that support the findings of this study are available from the corresponding author upon reasonable request.

Keywords

fluorescent nanoparticles, in vivo imaging, nanohybrids, polymer nanoparticles, shortwave infrared (SWIR)

Received: June 26, 2022

Revised: September 9, 2022

Published online: October 6, 2022

- a) X. Han, K. Xu, O. Taratula, K. Farsad, *Nanoscale* **2019**, *11*, 799; b) J. Elf, I. Barkefors, *Annu. Rev. Biochem.* **2019**, *88*, 635; c) L. J. Lauwerends, P. B. A. A. van Driel, R. J. Baatenburg de Jong, J. A. U. Hardillo, S. Koljenovic, G. Puppels, L. Mezzanotte, C. W. G. M. L wik, E. L. Rosenthal, A. L. Vahrmeijer, S. Keereweer, *Lancet Oncol.* **2021**, *22*, e186.
- S. Yoon, M. Kim, M. Jang, Y. Choi, W. Choi, S. Kang, W. Choi, *Nat. Rev. Phys.* **2020**, *2*, 141.
- E. Ximendes, A. Benayas, D. Jaque, R. Marin, *ACS Nano* **2021**, *15*, 1917.
- D. Dahal, P. Ray, D. Pan, *WIREs Nanomed. Nanobiotechnol.* **2021**, *13*, e1734.
- a) Z. Feng, T. Tang, T. Wu, X. Yu, Y. Zhang, M. Wang, J. Zheng, Y. Ying, S. Chen, J. Zhou, X. Fan, D. Zhang, S. Li, M. Zhang, J. Qian, *Light: Sci. Appl.* **2021**, *10*, 197; b) C. Paviolo, L. Cognet, *Neurobiol. Dis.* **2021**, *153*, 105328.
- a) S. Hatami, C. W rth, M. Kaiser, S. Leubner, S. Gabriel, L. Bahrig, V. Lesnyak, J. Pauli, N. Gaponik, A. Eychm ller, U. Resch-Genger, *Nanoscale* **2014**, *7*, 133; b) S. Zhu, R. Tian, A. L. Antaris, X. Chen, H. Dai, *Adv. Mater.* **2019**, *31*, 1900321.
- a) Y. Fan, F. Zhang, *Adv. Opt. Mater.* **2019**, *7*, 1801417; b) H. Lin, Z. Lin, K. Zheng, C. Wang, L. Lin, J. Chen, J. Song, *Adv. Opt. Mater.* **2021**, *9*, 2002177.
- a) H. PiwoŃski, Y. Wang, W. Li, T. Michinobu, S. Habuchi, *Nano Lett.* **2020**, *20*, 8803; b) Y. Zhu, Y. Miao, T. Xue, Y. Liu, C. Zheng, J. Ma, W. Tan, S. Wen, C. Gu, *J. Innovative Opt. Health Sci.* **2020**, *13*, 2041003; c) C. Gu, H. Wang, X. Wang, S. Wen, X. Liu, W. Tan, M. Qiu, J. Ma, *RSC Adv.* **2021**, *11*, 30798.
- a) W. Chen, C.-A. Cheng, E. D. Cosco, S. Ramakrishnan, J. G. P. Lingg, O. T. Bruns, J. I. Zink, E. M. Sletten, *J. Am. Chem. Soc.* **2019**, *141*, 12475; b) A. Yakovliev, R. Ziniuk, D. Wang, B. Xue, L.

- O. Vretik, O. A. Nikolaeva, M. Tan, G. Chen, Yu. L. Slominskii, J. Qu, T. Y. Ohulchanskyy, *Nanoscale Res. Lett.* **2019**, *14*, 243; c) O. M. Chepurna, A. Yakovliev, R. Ziniuk, O. A. Nikolaeva, S. M. Levchenko, H. Xu, M. Y. Losytskyy, J. L. Bricks, Yu. L. Slominskii, L. O. Vretik, J. Qu, T. Y. Ohulchanskyy, *J. Nanobiotechnol.* **2020**, *18*, 19.
- [10] a) J. Zheng, C. Zhou, M. Yu, J. Liu, *Nanoscale* **2012**, *4*, 4073; b) E. Porret, X. L. Guével, J.-L. Coll, *J. Mater. Chem. B* **2020**, *8*, 2216; c) Y. Xiao, Z. Wu, Q. Yao, J. Xie, *Aggregate* **2021**, *2*, 114.
- [11] H. Yu, B. Rao, W. Jiang, S. Yang, M. Zhu, *Coord. Chem. Rev.* **2019**, *378*, 595.
- [12] a) Y. Chen, D. M. Montana, H. Wei, J. M. Cordero, M. Schneider, X. L. Guével, O. Chen, O. T. Bruns, M. G. Bawendi, *Nano Lett.* **2017**, *17*, 6330; b) X. L. Guével, K. D. Wegner, C. Würth, V. A. Baulin, B. Musnier, V. Jossierand, U. Resch-Genger, J. Coll, *Chem. Commun.* **2022**, *58*, 2967.
- [13] a) H. Liu, G. Hong, Z. Luo, J. Chen, J. Chang, M. Gong, H. He, J. Yang, X. Yuan, L. Li, X. Mu, J. Wang, W. Mi, J. Luo, J. Xie, X.-D. Zhang, *Adv. Mater.* **2019**, *31*, 1901015; b) X. Song, W. Zhu, X. Ge, R. Li, S. Li, X. Chen, J. Song, J. Xie, X. Chen, H. Yang, *Angew. Chem.* **2021**, *133*, 1326; c) X. Song, W. Zhu, X. Ge, R. Li, S. Li, X. Chen, J. Song, J. Xie, X. Chen, H. Yang, *Angew. Chem., Int. Ed.* **2021**, *60*, 1306; d) S. Li, Q. Ma, C. Wang, K. Yang, Z. Hong, Q. Chen, J. Song, X. Song, H. Yang, *Anal. Chem.* **2022**, *94*, 2641.
- [14] B. Musnier, K. D. Wegner, C. Comby-Zerbino, V. Trouillet, M. Jourdan, I. Häusler, R. Antoine, J.-L. Coll, U. Resch-Genger, X. L. Guével, *Nanoscale* **2019**, *11*, 12092.
- [15] X. Kang, M. Zhu, *Chem. Soc. Rev.* **2019**, *48*, 2422.
- [16] a) A. Martino, S. A. Yamanaka, J. S. Kawola, D. A. Loy, *Chem. Mater.* **1997**, *9*, 423; b) X. L. Guével, B. Hötzer, G. Jung, M. Schneider, *J. Mater. Chem.* **2011**, *21*, 2974.
- [17] a) K. Selvaprakash, Y.-C. Chen, *Biosens. Bioelectron.* **2017**, *92*, 410; b) T. Geng, L. Zhao, D. Wu, H. Zhang, X. Zhao, M. Jiao, L. Zeng, *ACS Appl. Nano Mater.* **2021**, *4*, 13818.
- [18] a) F. Cao, E. Ju, C. Liu, W. Li, Y. Zhang, K. Dong, Z. Liu, J. Ren, X. Qu, *Nanoscale* **2017**, *9*, 4128; b) Y. Sun, T. Shu, J. Ma, Q. Dai, P. Peng, Z. Zhou, X. Zhou, L. Su, X. Zhang, *Anal. Chem.* **2022**, *94*, 3408.
- [19] a) W.-J. Chiu, W.-Y. Chen, H.-Z. Lai, C.-Y. Wu, H.-L. Chiang, Y.-C. Chen, *J. Nanopart. Res.* **2014**, *16*, 2478; b) A. M. Alkilany, S. Alstotari, M. Y. Alkawareek, S. R. Abulateefeh, *Sci. Rep.* **2019**, *9*, 11098.
- [20] a) D. Chen, Z. Luo, N. Li, J. Y. Lee, J. Xie, J. Lu, *Adv. Funct. Mater.* **2013**, *23*, 4324; b) E. R. Hebels, M. Najafi, J. van den Dikkenberg, N. Beztsinna, S. van de Looij, D. Wilbie, J. Meeldijk, M. Hembury, T. Vermonden, *Eur. Polym. J.* **2021**, *152*, 110467; c) Y. Li, S. Yi, Z. Lei, Y. Xiao, *RSC Adv.* **2021**, *11*, 14678.
- [21] a) Y. Hong, J. W. Y. Lam, B. Z. Tang, *Chem. Soc. Rev.* **2011**, *40*, 5361; b) A. Reisch, A. S. Klymchenko, *Small* **2016**, *12*, 1968.
- [22] a) N. Goswami, Q. Yao, Z. Luo, J. Li, T. Chen, J. Xie, *J. Phys. Chem. Lett.* **2016**, *7*, 962; b) A. Yahia-Ammar, D. Sierra, F. Mérola, N. Hildebrandt, X. L. Guével, *ACS Nano* **2016**, *10*, 2591.
- [23] a) S. M. D'Addio, R. K. Prud'homme, *Adv. Drug Delivery Rev.* **2011**, *63*, 417; b) C. J. Martínez Rivas, M. Tarhini, W. Badri, K. Miladi, H. Greige-Gerges, Q. A. Nazari, S. A. Galindo Rodríguez, R. Á. Román, H. Fessi, A. Elaissari, *Int. J. Pharm.* **2017**, *532*, 66.
- [24] a) V. Rosiuk, A. Runser, A. Klymchenko, A. Reisch, *Langmuir* **2019**, *35*, 7009; b) N. Melnychuk, S. Egloff, A. Runser, A. Reisch, A. S. Klymchenko, *Angew. Chem.* **2020**, *132*, 6878; c) N. Melnychuk, S. Egloff, A. Runser, A. Reisch, A. S. Klymchenko, *Angew. Chem., Int. Ed.* **2020**, *59*, 6811.
- [25] a) C. Zhang, V. J. Pansare, R. K. Prud'homme, R. D. Priestley, *Soft Matter* **2011**, *8*, 86; b) K. Roger, M. Eissa, A. Elaissari, B. Cabane, *Langmuir* **2013**, *29*, 11244; c) A. Reisch, A. Runser, Y. Arntz, Y. Mély, A. S. Klymchenko, *ACS Nano* **2015**, *9*, 5104; d) S. Egloff, A. Runser, A. Klymchenko, A. Reisch, *Small Methods* **2021**, *5*, 2000947.
- [26] Y. Li, S. Liu, T. Yao, Z. Sun, Z. Jiang, Y. Huang, H. Cheng, Y. Huang, Y. Jiang, Z. Xie, G. Pan, W. Yan, S. Wei, *Dalton Trans.* **2012**, *41*, 11725.
- [27] a) R. Jin, C. Zeng, M. Zhou, Y. Chen, *Chem. Rev.* **2016**, *116*, 10346; b) X. Kang, H. Chong, M. Zhu, *Nanoscale* **2018**, *10*, 10758.
- [28] S. Chandrasekhar, *Rev. Mod. Phys.* **1943**, *15*, 1.
- [29] R. Hoshi, K. Suzuki, N. Hasebe, T. Yoshihara, S. Tobita, *Anal. Chem.* **2020**, *92*, 607.
- [30] B. Andreiuk, A. Reisch, E. Bernhardt, A. S. Klymchenko, *Chem. - Asian J.* **2019**, *14*, 836.
- [31] J. A. Carr, D. Franke, J. R. Caram, C. F. Perkinson, M. Saif, V. Askoxylakis, M. Datta, D. Fukumura, R. K. Jain, M. G. Bawendi, O. T. Bruns, *Proc. Natl. Acad. Sci. USA* **2018**, *115*, 4465.
- [32] B. Li, M. Zhao, L. Feng, C. Dou, S. Ding, G. Zhou, L. Lu, H. Zhang, F. Chen, X. Li, G. Li, S. Zhao, C. Jiang, Y. Wang, D. Zhao, Y. Cheng, F. Zhang, *Nat. Commun.* **2020**, *11*, 3102.
- [33] Q. Li, C. J. ZemanIV, Z. Ma, G. C. Schatz, X. W. Gu, *Small* **2021**, *17*, 2007992.
- [34] Y. Li, M. Zha, G. Yang, S. Wang, J.-S. Ni, K. Li, *Chem. - Eur. J.* **2021**, *27*, 13085.
- [35] a) L.-J. Shi, C.-N. Zhu, H. He, D.-L. Zhu, Z.-L. Zhang, D.-W. Pang, Z.-Q. Tian, *RSC Adv.* **2016**, *6*, 38183; b) O. T. Bruns, T. S. Bischof, D. K. Harris, D. Franke, Y. Shi, L. Riedemann, A. Bartelt, F. B. Jaworski, J. A. Carr, C. J. Rowlands, M. W. B. Wilson, O. Chen, H. Wei, G. W. Hwang, D. M. Montana, I. Coropceanu, O. B. Achorn, J. Kloepper, J. Heeren, P. T. C. So, D. Fukumura, K. F. Jensen, R. K. Jain, M. G. Bawendi, *Nat. Biomed. Eng.* **2017**, *1*, 0056.
- [36] a) X. Le Guével, *IEEE J. Sel. Top. Quantum Electron.* **2014**, *20*, 45; b) Y. Huang, L. Fuksman, J. Zheng, *Dalton Trans.* **2018**, *47*, 6267.
- [37] N. Hildebrandt, in *FRET - Förster Resonance Energy Transfer* (Eds: I. L. Medintz, N. Hildebrandt), John Wiley & Sons, Ltd, New York **2013**, p. 105.
- [38] M. Zhou, Y. Song, *J. Phys. Chem. Lett.* **2021**, *12*, 1514.
- [39] Z. Luo, X. Yuan, Y. Yu, Q. Zhang, D. T. Leong, J. Y. Lee, J. Xie, *J. Am. Chem. Soc.* **2012**, *134*, 16662.
- [40] a) Z. Wu, Q. Yao, O. J. H. Chai, N. Ding, W. Xu, S. Zang, J. Xie, *Angew. Chem.* **2020**, *132*, 10020; b) Z. Wu, Q. Yao, O. J. H. Chai, N. Ding, W. Xu, S. Zang, J. Xie, *Angew. Chem., Int. Ed.* **2020**, *59*, 9934.
- [41] L. Lu, B. Li, S. Ding, Y. Fan, S. Wang, C. Sun, M. Zhao, C.-X. Zhao, F. Zhang, *Nat. Commun.* **2020**, *11*, 4192.
- [42] B. Musnier, M. Henry, J. Vollaie, J.-L. Coll, Y. Usson, V. Jossierand, X. L. Guével, *J. Biophotonics* **2021**, *14*, 202000345.
- [43] A. Combes, K. N. Tang, A. Klymchenko, A. Reisch, *J. Colloid Interface Sci.* **2022**, *607*, 1786.